Received: 26 October 2023 | Revised: 21 April 2024 | Accepted: 29 April 2024

DOI: 10.1002/mp.17180

RESEARCH ARTICLE

MEDICAL PHYSICS

Development and verification of an electron Monte Carlo engine for applications in intraoperative radiation therapy

Luisa Rank[1,2] | Peter Lysakovski[1] | Gerald Major[3] | Alfredo Ferrari[2] | Thomas Tessonnier[1] | Jürgen Debus[1,4,5] | Andrea Mairani[1,4,5,6,7]

[1] Heidelberg Ion-Beam Therapy Center (HIT), Department of Radiation Oncology, Heidelberg University Hospital, Heidelberg, Germany

[2] Karlsruhe Institute of Technology (KIT), Faculty of Physics, Karlsruhe, Germany

[3] Department of Radiation Oncology, Heidelberg University Hospital, Heidelberg, Germany

[4] Heidelberg Institute of Radiation Oncology (HIRO), National Center for Radiation Oncology (NCRO), Heidelberg University Hospital (UKHD), Heidelberg Faculty of Medicine (MFHD) and German Cancer Research Center (DKFZ), Heidelberg, Germany

[5] Clinical Cooperation Unit Translational Radiation Oncology, German Cancer Consortium (DKTK) Core-Center Heidelberg, National Center for Tumor Diseases (NCT), Heidelberg University Hospital (UKHD) and German Cancer Research Center (DKFZ), Heidelberg, Germany

[6] Division of Molecular and Translational Radiation Oncology, Heidelberg Faculty of Medicine (MFHD) and Department of Radiation Oncology, Heidelberg University Hospital (UKHD), Heidelberg, Germany

[7] Medical Physics, National Centre of Oncological Hadrontherapy (CNAO), Pavia, Italy

Correspondence
Andrea Mairani, Heidelberg Ion-Beam Therapy Center (HIT), Department of Radiation Oncology, Heidelberg University Hospital, Heidelberg, Germany.
Email:
Andrea.Mairani@med.uni-heidelberg.de

Funding information
German Federal Ministry of Education and Research (BMBF), Grant/Award Number: 13GW0436A

Abstract

Background: In preparation of future clinical trials employing the Mobetron electron linear accelerator to deliver FLASH Intraoperative Radiation Therapy (IORT), the development of a Monte Carlo (MC)-based framework for dose calculation was required.

Purpose: To extend and validate the in-house developed fast MC dose engine MonteRay (MR) for future clinical applications in IORT.

Methods: MR is a CPU MC dose calculation engine written in C++ that is capable of simulating therapeutic proton, helium, and carbon ion beams. In this work, development steps are taken to include electrons and photons in MR are presented. To assess MRs accuracy, MR generated simulation results were compared against FLUKA predictions in water, in presence of heterogeneities as well as in an anthropomorphic phantom. Additionally, dosimetric data has been acquired to evaluate MRs accuracy in predicting dose-distributions generated by the Mobetron accelerator. Runtimes of MR were evaluated against those of the general-purpose MC code FLUKA on standard benchmark problems.

Results: MR generated dose distributions for electron beams incident on a water phantom match corresponding FLUKA calculated distributions within 2.3% with range values matching within 0.01 mm. In terms of dosimetric validation, differences between MR calculated and measured dose values were below 3% for almost all investigated positions within the water phantom. Gamma passing rate (1%/1 mm) for the scenarios with inhomogeneities and gamma passing rate (3%/2 mm) with the anthropomorphic phantom, were $>$ 99.8% and 99.4%,

---

Luisa Rank and Peter Lysakovski contributed equally to this study.

respectively. The average dose differences between MR (FLUKA) and the measurements was 1.26% (1.09%). Deviations between MR and FLUKA were well within 1.5% for all investigated depths and 0.6% on average. In terms of runtime, MR achieved a speedup against reference FLUKA simulations of about 13 for 10 MeV electrons.

Conclusions: Validations against general purpose MC code FLUKA predictions and experimental dosimetric data have proven the validity of the physical models implemented in MR for IORT applications. Extending the work presented here, MR will be interfaced with external biophysical models to allow accurate FLASH biological dose predictions in IORT.

KEYWORDS

electron, engine, intraoperative, mobetron, Monte Carlo, MonteRay, radiotherapy

1 | INTRODUCTION

Cancer is one of the leading causes of death worldwide. In 2020, almost 10 million cancer deaths were registered.[1] One of the most important treatment options for cancer patients is radiotherapy, alongside chemotherapy and surgery.[2] Approximately half of all cancer patients undergo radiation therapy throughout the course of their disease.[3] Typically, deep seated tumors are treated with photon beams. However, for shallow tumors such as tumors of the skin or intra-operative applications, electron beams are widely used in medical centers. Their well-defined range in body tissue and sharp distal dose fall-off enables the treatment of cancerous tissue close to the surface, while sparing underlying organs at risk.[4]

Intraoperative Radiation Therapy (IORT) systems operating at FLASH dose-rates such as the Mobetron linear electron accelerator (IntraOp Medical Corporation, Sunnyvale, CA)5 could additionally widen the therapeutic window with a potential decrease in the normal tissue toxicity. The so-called FLASH effect has been observed for high dose (> about 8 Gy) and high dose-rate (about 40 Gy/s) with an increased normal tissue sparing at similar tumor control.[6–8]

At the Department of Radiation Oncology in Heidelberg, biophysical investigations and future clinical trials are planned to evaluate the clinical potential of FLASH IORT using the available Mobetron linear electron accelerator. To support these developments, the UNIVERSE (UNIfied and VERSatile bio response Engine) biological model[9–11] has been extended for FLASH radiotherapy applications while fast and accurate calculation tools for the absorbed dose are not yet available.

The radiation dose deposited within the patient's body is usually determined via analytical algorithms or Monte Carlo (MC) calculations. General purpose MC engines such as FLUKA,[12–14] GEANT4,[15,16] PENELOPE[17,18], and EGSnrc[19] are considered the gold standard in terms of accuracy.[20] However, classical MC codes are constrained by their high computation times which limit their application for a fast pre-IORT dose computation using in room computed tomography (CT) for patient positioning verification. To that end, fast MC frameworks like MonteRay[21–23] have been introduced recently, focusing on both accuracy and simulation speed. MonteRay (MR), developed at the Heidelberg Ion-Beam Therapy Center (HIT) by Lysakovski et al.,[21–23] currently supports dose calculations for protons, helium ions, and carbon ions. This work presents the development and verification of an electron dose engine for radiation therapy applications, integrated into the existing MC framework MR. To benchmark the engine's accuracy and performance, an extensive verification against FLUKA simulations was performed. To further benchmark MR, dosimetric data was acquired using a Mobetron electron linear accelerator (9 MeV) and compared to simulation results.

2 | MATERIAL AND METHODS

The subsequent sections provide detailed information on the methods used to extend the MR framework, on the benchmarks performed against FLUKA and on the experimental characterization of the Mobetron electron linear accelerator. A thorough description of the concepts and code structure of MR can be found in.[21–23] A summary of the physical models employed and tabulated quantities for each implemented process is presented in Table 1.

2.1 | Continuous electromagnetic interactions

2.1.1 | Mean energy loss

The mean energy loss for each simulation step is calculated based on tabulated stopping power values, as is described in detail in ref. 23 The stopping power database table for electron beams was generated by extracting restricted stopping power values for electrons in water from FLUKA. During the extraction process, a

TABLE 1 Summary of the employed models and tabulated quantities for each implemented process.

Process	Source	Tabulated quantities
Mean energy loss	FLUKA	Stopping power in water, stopping power ratios for other compounds
Energy straggling	Chibani et al.[24]	Material constants (density, elemental composition, etc.)
Multiple scattering	Approximation to Molière according to Lysakovski et al.[22]	Material constants (density, elemental composition, etc.)
Møller scattering	Cross sections after Sempau[28] kinematics after Salvat and Fernandez-Varea[29]	Pre-computed cross-sections and material constants
Bremsstrahlung	Cross sections after Seltzer and Berger,[30] Sampling of photon energies after Wasaye et al.,[31] Sampling of deflection angle after GEANT4[16]	Tabulated cross sections from Seltzer and Berger
Photoelectric effect	Cross section from the National Institute of Standards and Technology (NIST) [97] with local energy deposition	Cross sections
Compton scattering	Cross sections from NIST [97] sampling following the approach of GEANT4[16]	Cross sections
Pair production	Cross sections from NIST [97] after PENELOPE[18] with custom sampling routine	Cross sections and fit parameters for custom sampling routine

kinetic energy threshold of 0.1 MeV for delta-ray production was used in FLUKA. The stopping power was tabulated for $N = 10\,000$ kinetic energy values between $E_{\min} = 0.1$ MeV and $E_{\max} = 500$ MeV. Intervals between successive table entries were chosen using

$$E_n = 2^{m \cdot n + b}$$

with

$$m = \frac{\log_2\left(\frac{E_{max}}{E_{min}}\right)}{N-1}$$

and

$$b = \log_2\left(E_{min}\right)$$

to ensure high resolution for low energies, where the stopping power changes rapidly as a function of the energy, while avoiding overly detailed binning for high energies.

2.1.2 | Energy loss straggling

Energy loss straggling was implemented following an approach suggested by Chibani[24] using simple energy loss sampling functions. Either a Gaussian, a log-normal, or a Landau distribution is chosen according to the value of $\varkappa$, which is defined as

$$\varkappa = \frac{\xi}{dE_{max}}$$

with

$$\xi = 2\pi \cdot N_a m {r_e}^2 \rho \cdot dx \cdot \frac{q^2}{e^2} \frac{Z}{A} \frac{1}{\beta^2},$$

where N_a is Avogadro's number, m the electron mass, r_e the classical electron radius, q the particle's charge, Z the target's atomic number and A the target's mass number. According to Pauli's exclusion principle,[25] $dE_{\max}$ is equal to $E_0/2$ for electrons where E_0 is the electron kinetic energy. However, restricted stopping powers were employed, which means that energy losses above the delta-ray production threshold are assumed to occur as discrete energy losses with secondary electron production. Consequently, the maximum energy transfer was defined via the delta-ray production threshold for electrons.

2.1.3 | Multiple coulomb scattering

MRs scattering model builds upon the theoretical description of multiple scattering processes by Molière.[26] Since sampling from Molière's scattering distribution comes with significant computational costs, an approximation of Molière's distribution function, where small angles and asymptotically large angles are treated separately, is used, as suggested by Kuhn and Dodge.[27] A thorough description of the treatment of continuous scattering processes can be found in ref. 22

2.2 | Discrete electron specific interactions

Møller scattering and bremsstrahlung were implemented to enable electron beam calculations. For each simulation step, the distance to the next discrete electron specific interaction is sampled from an exponential distribution, using precalculated cross section tables. The cross-section database table for electrons was generated by tabulating the total mean free path. When a discrete interaction occurs, the interaction type, either Møller scattering or bremsstrahlung, and the interacting atom, are chosen according to the probabilities for the respective interactions. Those probabilities were precomputed and tabulated alongside the total mean free path for each row in the database table. Detailed information on the implementation of Møller scattering and bremsstrahlung can be found below.

2.2.1 | Møller scattering

Inelastic collisions of electrons with atomic electrons are approximated as Møller interactions, that is, as inelastic collisions of electrons with free electrons at rest. The differential cross section per atom for those interactions is given by[28]

$$\frac{d\sigma_{M\tau ller}(k)}{dk} = \frac{2\pi e^4}{mv^2}\,\frac{Z}{Ek^2}\left(1+\left(\frac{k}{1-k}\right)^2-\frac{k}{1-k}\right.$$
$$\left.+\left(\frac{\gamma-1}{\gamma}\right)^2\left(k^2+\frac{k}{1-k}\right)\right)$$

with

$$k=\frac{W}{E}$$

and

$$\gamma=\frac{E+mc^2}{mc^2},$$

where e refers to the elementary charge, m to the mass of the projectile and v to its speed. E denotes the kinetic energy of the projectile prior to the scattering process, W its energy loss due to the inelastic interaction and Z the atomic number of the target material. Since the final state particles are both electrons, they are indistinguishable. Consequently, the parameter k cannot be larger than 0.5.

The total cross section per atom can be derived from the differential cross section via integration[28]:

$$\sigma^Z_{M\tau ller} = \frac{mv^2}{2\pi e^4}\,\frac{E}{Z}\left(\frac{1-2k_c}{k_c(1-k_c)}+\left(\frac{\gamma-1}{\gamma}\right)^2\left(\frac{1}{2}-k_c\right)\right.$$
$$\left.+\left(\left(\frac{\gamma-1}{\gamma}\right)^2-1\right)ln\frac{1-k_c}{k_c}\right)^{-1}.$$

Here, k_c refers to the lower integration limit

$$k_c=\frac{W_c}{E}.$$

The cutoff value W_c was set to 0.1 MeV, such that it corresponds to the kinetic energy threshold for delta-ray production, employed to determine the restricted stopping power. As a result, the total cross section is defined for projectile energies above 0.2 MeV.

When the Møller routine is executed, a secondary electron (delta-ray) is generated. The energy of the newly generated particle, which corresponds to the energy loss of the projectile, is then determined via sampling from the normalized probability density function (PDF)

$$P\ (k) = \frac{1}{k^2}\left(1+\left(\frac{k}{1-k}\right)^2-\frac{k}{1-k}\right.$$
$$\left.+\left(\frac{\gamma-1}{\gamma}\right)^2\left(k^2+\frac{k}{1-k}\right)\right)\cdot\theta\,(k-k_c)\cdot\theta\left(\frac{1}{2}-k\right)$$

using a combination of the composition method and the acceptance rejection method, as suggested by Salvat and Fernández-Varea.[29] Based on the sampled energy loss, the deflection angles are derived via energy and momentum conservation.

2.2.2 | Bremsstrahlung

The differential cross section for bremsstrahlung, that is, the generation of a secondary photon during the deflection of an electron by a nucleus, can be written as[30]

$$\frac{\beta^2}{Z^2}Z\,\frac{d\sigma_{Brems}}{dW} = \chi\left(Z,E,k=\frac{W}{E}\right),$$

where Z is the atomic number of the nucleus, E the kinetic energy of the incident electron, W its energy loss (which corresponds to the energy of the generated photon) and β the incident electron's velocity in units of the speed of light. χ refers to the so-called scaled differential cross section for bremsstrahlung. The total cross section as a function of E for a given value of Z can be derived from the scaled differential cross section via integration:

$$\sigma^Z_{Brems}(E)=\int_{W_c}^{E}\frac{Z^2}{\beta^2 W}\chi^Z(W)dW.$$

Here, the lower integration limit W_c corresponds to the energy threshold for bremsstrahlung, which was set to 0.033 MeV.

Tabulated values of the scaled differential cross section per atom in terms of Z and k can be found in work by Seltzer and Berger.[30] Using those tabulated values, the total cross sections per atom were derived via numerical integration according to the equation above.

Intermediate data points were obtained through linear interpolation of the tabulated scaled differential cross section values in ln(W).

As suggested by Wasaye et al.,[31] the energy loss fraction k due to a bremsstrahlung interaction is sampled from the PDF

$$P\,(k) = \frac{1}{k}\,\chi(Z, E, k).$$

The deflection angle θ cannot be calculated from the sampled energy loss fraction via energy and momentum conservation. Therefore, a sampling algorithm similar to the algorithm employed in GEANT4[18] was implemented. As suggested in the GEANT4 manual, the electron deflection angle is chosen randomly from the PDF

$$P\,(u) = \frac{9\alpha^2}{9+\beta}\,\left(u \cdot exp\,exp\,\left(-\alpha u\right)\, + \beta u \cdot exp\,exp\,\left(-3\alpha u\right)\,\right)$$

with

$$u\; = \frac{E\theta}{m}\,,\; \alpha\; = \;0.625\;and\;\beta\; = \;27,$$

where m is the electron mass and E is the kinetic energy of the incident electron in GeV. The azimuthal angles for the deflected electron and the newly generated photon are determined via sampling from a uniform distribution over $[0, 2\pi)$.

2.3 | Discrete photon specific interactions

Three distinct photon specific interactions were implemented within MR to enable photon beam calculations for medical applications: photoelectric absorption, Compton scattering and pair production. Similar to electron specific interactions, the distance to the next photon specific interaction as well as its type are determined from tabulated cross section values during runtime. To generate the respective database for photons, macroscopic cross section tables for the distinct interactions were extracted from NIST XCOM.[32] Based on the NIST cross section values, the total mean free path for photons and the corresponding probabilities for the three photon specific interactions were tabulated.

2.3.1 | Photoelectric absorption

As photoelectric absorption processes are only relevant for low energies and high atomic numbers, they are approximated through local energy depositions, following the approach of Sempau et al..[28] When a photon enters the photoelectric absorption routine, its transport is aborted and its energy is deposited at the position, where the interaction took place.

2.3.2 | Compton scattering

During runtime, the energy loss of photons due to Compton interactions is sampled from the PDF

$$P\,\left(\epsilon = \frac{E_{\gamma'}}{E_\gamma}\right) = \left(\frac{1}{\epsilon} + \epsilon\right)\,\left(1 - \frac{\epsilon\theta}{1+\epsilon^2}\right),$$

which can be derived from the Klein-Nishina differential cross section for Compton processes.[33] Here, E_γ refers to the initial photon energy and $E_{\gamma'}$ to the photon energy after the scattering event. To determine random values from the PDF, a combination of the composition method and the acceptance rejection method is used, as suggested in the GEANT4 manual.[16]

To calculate the deflection angle θ, the Compton formula

$$E_{\gamma'} = E_\gamma\,\frac{mc^2}{mc^2 + E_\gamma\,(1 - cos\,cos\,\theta\,)}$$

is used, which can be derived via energy and momentum conservation under the assumption of an elastic collision. The secondary electron's direction of movement is given by[16]

$$cos\,cos\,\theta'\; = \frac{E_\gamma - E_{\gamma'}\,cos\,cos\,\theta}{\sqrt{E_\gamma^2 + E_{\gamma'}^2 - 2E_\gamma E_{\gamma'}\,cos\,cos\,\theta}}\;.$$

The azimuthal angles for the final state particles are drawn from a uniform distribution over $[0, 2\pi)$.

2.3.3 | Pair production

When a pair production process occurs, the incident photon is absorbed, that is, its energy is set to zero, and two secondary particles are generated. As suggested by Sempau et al.,[28] two electrons, in the following referred to via the indices 1 and 2, are produced instead of an electron positron pair. As a result, differences between electrons and positrons in terms of cross sections and stopping powers are ignored. This simplification is considered valid, since the impact of these differences on dose calculations is negligible in the context of low-energy electron beam calculations for radiation therapy applications.[28]

Following the approach to pair production employed in the PENELOPE framework,[18] which is based on work by Baró et al.,[17] the reduced energy

$$\epsilon\; = \frac{E_1 + mc^2}{E_\gamma}$$

is determined via sampling from the PDF

$$P\ (\epsilon) = 2\left(\frac{1}{2} - \epsilon\right)^2 \phi_1(\epsilon) + \phi_2(\epsilon),$$

which is derived from the Bethe-Heitler differential cross section for pair production processes.[34,35] Here, m refers to the electron mass, E_1 to the kinetic energy of the secondary electron with index 1, c to the speed of light and E_γ to the initial photon energy. ϕ_1 and ϕ_2 are functions of the reduced energy and a detailed description of them can be found in the PENELOPE manual.[18] Deviating from the PENELOPE approach, a simple acceptance rejection method was implemented to determine random values from the PDF. Therefore, the required proposal function Υ was chosen as follows:

$$\Upsilon\ (E_\gamma) = \left(\frac{E_\gamma}{a_Z}\right)^{\frac{1}{4}}$$

Here, a_Z refers to the atomic number dependent parameter, as reported in Table S1. Random values of ϵ are generated from the proposal function via the following algorithm:

1. Sample a random value of ϵ from a uniform distribution over $[\epsilon_{min},\ \epsilon_{max}]$ with

$$\epsilon_{min} = \frac{mc^2}{E_\gamma}$$

and

$$\epsilon_{max} = 1 - \frac{mc^2}{E_\gamma}.$$

2. Compute $\Upsilon(E_\gamma)$ and $P(\epsilon)$.
3. Sample a random number ξ from a uniform distribution over [0,1).
4. If $P(\epsilon) \geq \xi\ \Upsilon(E_\gamma)$, deliver ϵ.
5. Go back to 1.

For example, for $Z = 1$ and $E_\gamma = 10$ MeV, the efficiency of the algorithm, that is, the probability for ϵ being accepted in Step 4, is approximately 65%.

Based on the sampled value of ϵ, the kinetic energies of the secondary electrons can be calculated via

$$E_1 = \epsilon E_\gamma - mc^2$$

and

$$E_2 = E_\gamma\ - E_1 - 2mc^2.$$

Since the final state not only involves the secondary electrons but also a nucleus, the secondary electrons' directions of movement cannot be calculated in a straightforward manner from their kinetic energies via energy and momentum conservation.[18] Consequently, a sampling algorithm was implemented to determine those directions. As suggested in the PENELOPE manual,[18] the polar angles θ_1 and θ_2 between the electrons' directions of movement and the photon's velocity are sampled from "the leading term of the expression obtained from high-energy theory[18,36,37]

$$P\ \left(cos\,cos\,\theta_{1,2}\ \right) = a\left(1 - \beta_{1,2}cos\,cos\,\theta_{1,2}\ \right)^{-2}$$

with

$$\beta_{1,2} = \frac{\sqrt{E_{1,2}(E_{1,2} + 2mc^2)}}{E_{1,2} + mc^2}$$

where a is a normalization constant. Concerning the azimuthal angles, no limitations have to be considered. Consequently, they are chosen randomly from a uniform distribution over $[0, 2\pi)$ for both final state electrons.

2.4 | Verification against FLUKA calculations in water

To assess MRs accuracy concerning electron beam calculations, MR generated simulation results were compared against FLUKA predictions. During the verification process, all FLUKA simulations were executed with kinetic energy thresholds of 0.1 and 0.033 MeV for delta-ray production and bremsstrahlung, respectively. For both MC engines, the electron transport threshold was set to 0.1 MeV. For photons, a transport threshold of 0.033 MeV was employed. The energy loss fraction per step was limited to 5% during simulation setup.

To gauge the accuracy of the physical models implemented within MR, considering continuous energy loss processes and Multiple Coulomb Scattering, calculations were done for pencil-like electron beams with a representative initial energy of 10 MeV incident on a thin water slab. To that end, energy loss and deflection angle distributions were computed with MR and FLUKA for electrons exiting the water slab. To quantify the level of agreement between MR and FLUKA, ratios between the respective distributions were determined for each distribution bin. In addition to that, relative differences in mean energy loss and deflection angle values were evaluated.

With the purpose of verifying the developed electron dose engine against FLUKA, integrated depth dose (IDD) distributions and lateral dose profiles were generated for electrons with initial energies of 5 and 10 MeV impinging on a voxelized water target. Since photon interactions were implemented during the development of the electron dose engine as well, the same was done for photons as beam particles. The corresponding results can be found in the supplementary material (Figure S2) together with the scoring settings (Table S2). To avoid boundary effects, the particles were generated within the water target at $z = 0$ cm with a primary momentum directed along the z-axis for all simulations. Pencil-like beams, that is, beams that originate from a point-like source, were employed for electrons. As the range of particles in water is dependent on their initial energy, the target and voxel dimensions were varied with the particle energy. For 5 (10) MeV electron beam a scoring volume of 10 × 10 × 4 cm^3 (20 × 20 × 8 cm^3) was used with voxel size of 0.05 × 0.05 × 0.025 cm^3 (0.1 × 0.1 × 0.05 cm^3). To quantify differences in the dose distributions obtained with MR and FLUKA, the global dose difference

$$Dd = \frac{D_{MonteRay} - D_{FLUKA}}{D_{FLUKA}^{max}}$$

was computed for each distribution bin. Besides that, the therapeutic ranges, that is, the R_{80} depths (distal depth at which the dose reached the 80% of the peak) were calculated for electrons, using both MC engines.

2.5 | Verification against FLUKA calculations with heterogeneities

With the purpose of verifying the developed electron dose engine against FLUKA in presence of heterogeneities, we have performed simulations using a water phantom including lung (0.26 g/cm^3) and bone (1.58 g/cm^3) inserts. The insert was a parallelepiped of 1 × 1 × 1.8 cm^3 (beam-eye view section: 1 × 1 cm^2). A 10 MeV electron square field of 4 × 4 cm^2 covering the insert was used as a beam. For both MC engines, simulations have been performed using 10^8 primary electrons and the results expressed in Gy/primary (dose-to-medium) were multiplied by $5–10^{10}$. A scoring volume of 12 × 12 × 9 cm^3 with a voxel size of 0.1 × 0.1 × 0.05 cm^3 was used. To quantify the agreement between MR and FLUKA, local 3D-γ analysis was carried out using the python package pymedphys (version 0.34.0) with a 1%/1 mm a criterion and a low dose threshold of 5%.

For additional verification in heterogeneous conditions, an anthropomorphic head phantom (Alderson phantom Radiology Support Devices, Long Beach, CA, USA) was used. The head phantom CT was translated in a voxelized MR geometry as described previously.[21–23] A 10 MeV electron square field of 8 × 8 cm^2 was used as a beam. For both MC engines, simulations have been performed using $4–10^8$ primary electrons and the results expressed in Gy/primary (dose-to-medium) were multiplied by $2–10^{11}$. Scoring was performed on the original CT using native voxel size of 0.06 × 0.06 × 0.3 cm^3. To quantify the agreement between MR and FLUKA, local 3D-γ passing rate was calculated with a 3%/2 mm a criterion and a low dose threshold of 5%.

Initially, for both MC engines the transport and production thresholds were kept the same as described in Section 2.4. In order to additionally verify MR approximations, FLUKA electron production and transport thresholds were lowered to 10 keV for the set-ups with lung and bone inserts.

2.6 | Experimental verification

2.6.1 | Experimental setup

Experimental data was taken using a Mobetron linear electron accelerator[5] in conjunction with PTW (Freiburg, Germany) dosimetry equipment. The Mobetron accelerator is a medical linear accelerator specifically designed for applications in intraoperative electron beam therapy. The accelerator used in the context of this work is a modified version of the Mobetron, that provides two different dose rate modes.[38] In addition to conventional dose rates, the modified version is also able to generate ultra-high dose rates for research purposes. Within the scope of this work, the Mobetron was exclusively used in conventional mode with dose rates of approximately 10 Gy per minute and a beam energy of 9 MeV. For conventional dose rate settings, the accelerator generates electron pulses with a pulse width of 1.2 μs and a pulse frequency of 30 Hz. As a detector, the PTW diode *E* (Type 60017) was used. The sensitive volume of the diode is disc-shaped with a lateral extent of 1 mm^2 and a thickness of 30 μm.

To characterize the dose distribution in a water phantom (PTW MP3-XS), positioned directly after the Mobetron head, a central axis depth dose curve as well as multiple lateral dose profiles were obtained. Regarding the depth dose curve, data points were collected for depths in water ranging from 3 to 60 mm with a distance of 1 mm between successive measurements. As for the lateral profiles, six different depths in water were investigated; 3, 10, 15, 20, 25, and 37 mm. Dose measurements were taken for lateral positions spanning from -60 to 60 mm at intervals of 1 mm. During the measurements, the water phantom was positioned such that the water surface was in contact with the distal end of the Mobetron head.

2.6.2 | Modeling of the Mobetron electron linear accelerator head

To enable dose calculations for Mobetron generated electron beams in MR, a beam model specific to the

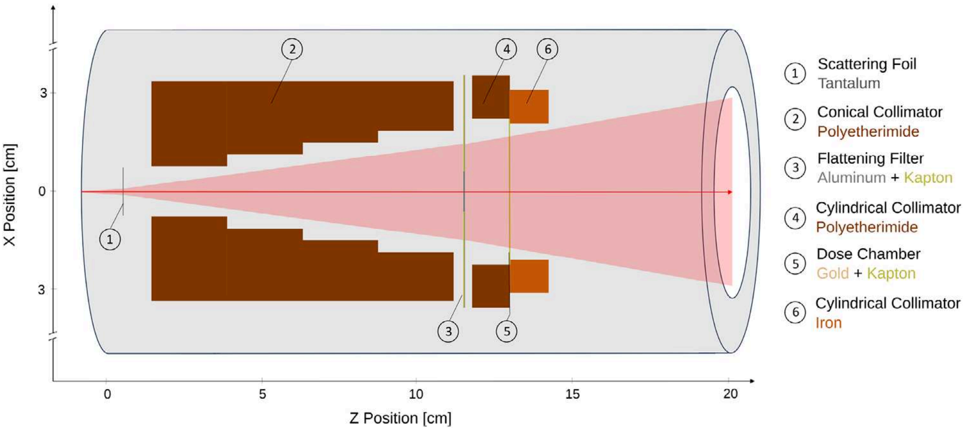

FIGURE 1 Schematic visualization of the simplified Mobetron radiation head geometry, implemented within FLUKA.

accelerator head was integrated into the MC framework through an external phase-space generated using FLUKA. Based on geometry information provided by the manufacturer, a simplified version of the radiation head geometry was integrated into FLUKA simulations. Particle types, energies and velocities for all particles exiting the radiation head were then extracted from FLUKA during runtime.

A schematic visualization of the geometry employed to generate the phase-space file is shown in Figure 1. A dose chamber with gold-plated electrodes enables beam monitoring during irradiation and multiple collimators made of polyetherimide (ρ = 1.27 g/cm^3) and iron are used to focus the electron beam. The most important components with regards to shaping the beam are a scattering foil made of tantalum and a flattening filter consisting of two disc-shaped aluminum plates.

2.6.3 | Benchmarks against dosimetric data

To test the implemented beam model of the Mobetron head and MR performances, dose distributions for particles sampled from the phase-space file impinging on a water phantom were generated with MR and evaluated against the experimental data and FLUKA simulations. During simulation setup, the energy thresholds for particle transport, delta-ray production and bremsstrahlung were set according to Section 2.4. The energy loss fraction per step was limited to 1% for both MC engines. With regards to the detector size, voxels with dimensions of $1 \times 1 \times 1$ mm^3 were used to score the deposited energy. To quantify differences between the MC derived and measured dose distributions, the global dose difference was employed. Moreover, therapeutic ranges were calculated based on the MR simulated, FLUKA generated and measured depth dose curves.

3 | RESULTS

3.1 | Verification against FLUKA calculations

3.1.1 | Thin water slab calculations

Energy loss and deflection angle distributions were simulated with MR and FLUKA for 10 MeV electrons impinging on thin water slabs of 1 mm and 1 cm thickness. To obtain the simulation results, 10 particle beams with 10^5 primary particles each were used for all configurations. In Figure 2, the results are shown for water slabs of 1 mm (panels (a) and (c)) and 1 cm (panels (b) and (d)) thickness. In general, the MR derived energy loss and deflection angle distributions show good agreement with the FLUKA generated data. After 1 mm of water, the difference in the mean energy loss is within the statistical uncertainties with 0.0 ± 1.5% (Figure 2a). However, discrepancies between MR and FLUKA in the angular distribution for intermediate deflection angles (Figure 2b) lead to a difference of 2.7 ± 0.6% in θ_{mean}. The MR generated simulation results after 1 cm of water demonstrates an improved level of agreement with the FLUKA generated data. The difference in the mean energy loss value is close to zero (Figure 2c) and the MR and FLUKA derived results are compatible with each other considering the uncertainties (difference of 0.3 ± 0.4% in θ_{mean}). Deviations between the MC engines in the deflection angle are still noticeable. In comparison to the simulation results after 1 mm of water though, significant improvement concerning the discrepancy in the mean deflection angle is found with a relative difference of −1.7 ± 0.4%.

3.1.2 | Water phantom calculations

IDD curves and lateral dose profiles were generated for electron beams incident on a homogeneous water

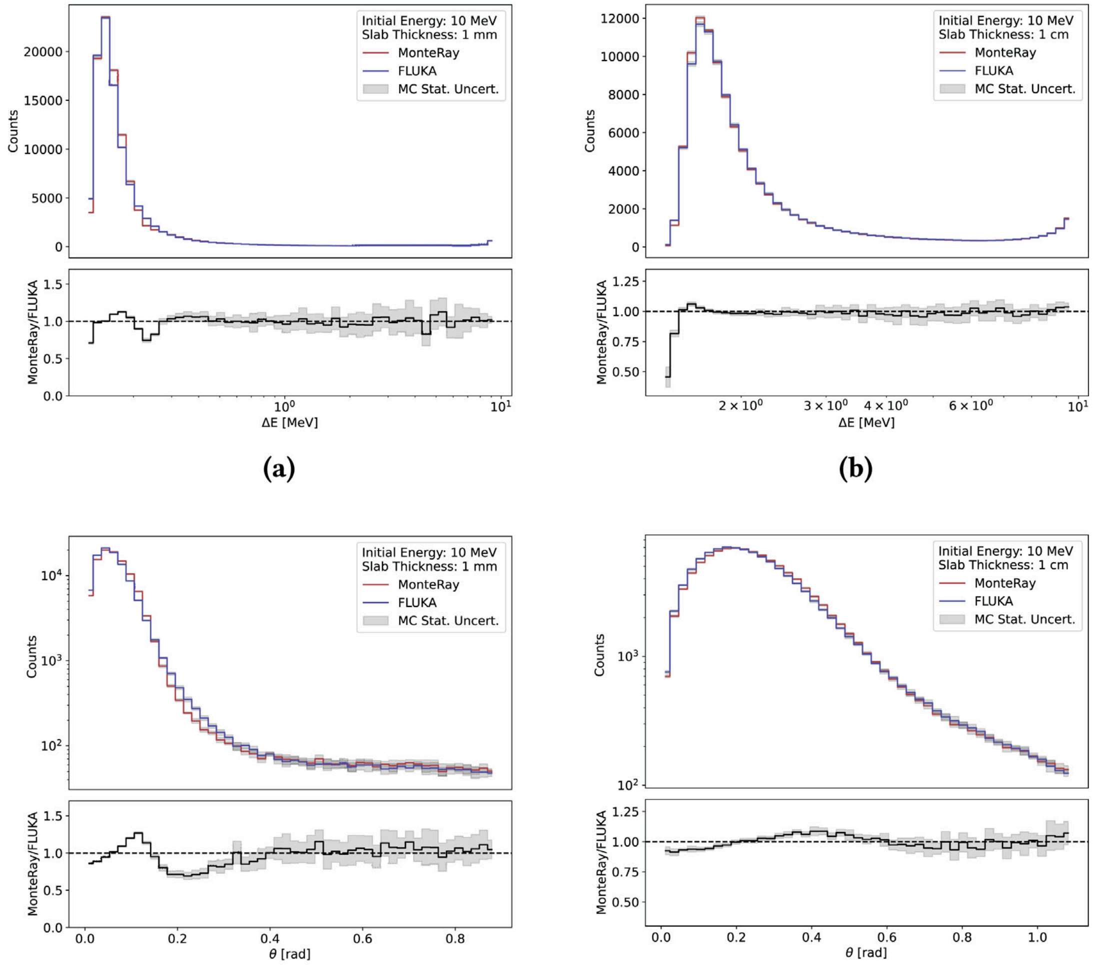

(a) (b)

(c) (d)

FIGURE 2 Energy loss and deflection angle distributions of 10 MeV electrons after 1 mm and 1 cm of water. The simulations have been performed 10 times using 10^5 primary electrons with MR and FLUKA. Panel (a): Energy loss distribution and corresponding ratio plot in the 99% quantile after 1 mm of water. Panel (b): Energy loss distribution and corresponding ratio plot in the 99% quantile after 1 cm of water. Panel (c): Deflection angle distribution and corresponding ratio plot in the 99% quantile after 1 mm of water. Panel (d): Deflection angle distribution and corresponding ratio plot in the 99% quantile after 1 cm of water. MR, MonteRay.

phantom with MR and FLUKA. Two distinct initial particle energies were studied: 5 and 10 MeV. All presented results are derived from simulations with 10^6 primary particles.

In Figure 3a, the IDD curves obtained with MR and FLUKA for incident electrons with an initial energy of 5 MeV are displayed. Figure 3b shows the corresponding lateral profiles at the depth where the maximum dose is obtained (R_{100}), that is, at approximately 1.2 cm. The results clearly demonstrate a high level of agreement between the MR and FLUKA generated data. The dose difference ranges from –0.9% to 1.5% in the depth dose curve around a relative average absolute value of 0.5%. The MR and FLUKA calculated therapeutic ranges (R_{80}) agree to within 0.01 mm. As for the lateral profiles, dose differences vary between –0.5% and 1.6%, with a mean difference of 0.2%.

In Figure 3c,d, the results for incident electron beams with an initial energy of 10 MeV are shown. Again, the lateral profile is displayed for the R_{100} depth, that is, at approximately 2.8 cm. The dose differences are within 2.3% for all data points, varying between –1.1% and 1.0% for the depth dose curves and between –0.7% and 2.3% for the lateral profiles. The mean dose differences are 0.3% and 0.2%, respectively. As for the therapeutic range (R_{80}), the MR derived value again agrees to within 0.01 mm to the FLUKA calculated counterpart. Statistical uncertainties are in the same order of magnitude for MR and FLUKA and they are not visualized in the figure as they are below 1%.

3.1.3 | Calculations with heterogeneities

In Figure 4 (5), MR and FLUKA 2D dose distributions are overlaid over the geometry consisting of a water tank with a lung (bone) insert. The 10 MeV electron beam (4×4 cm^2 field) impinges from the left of the water tank.

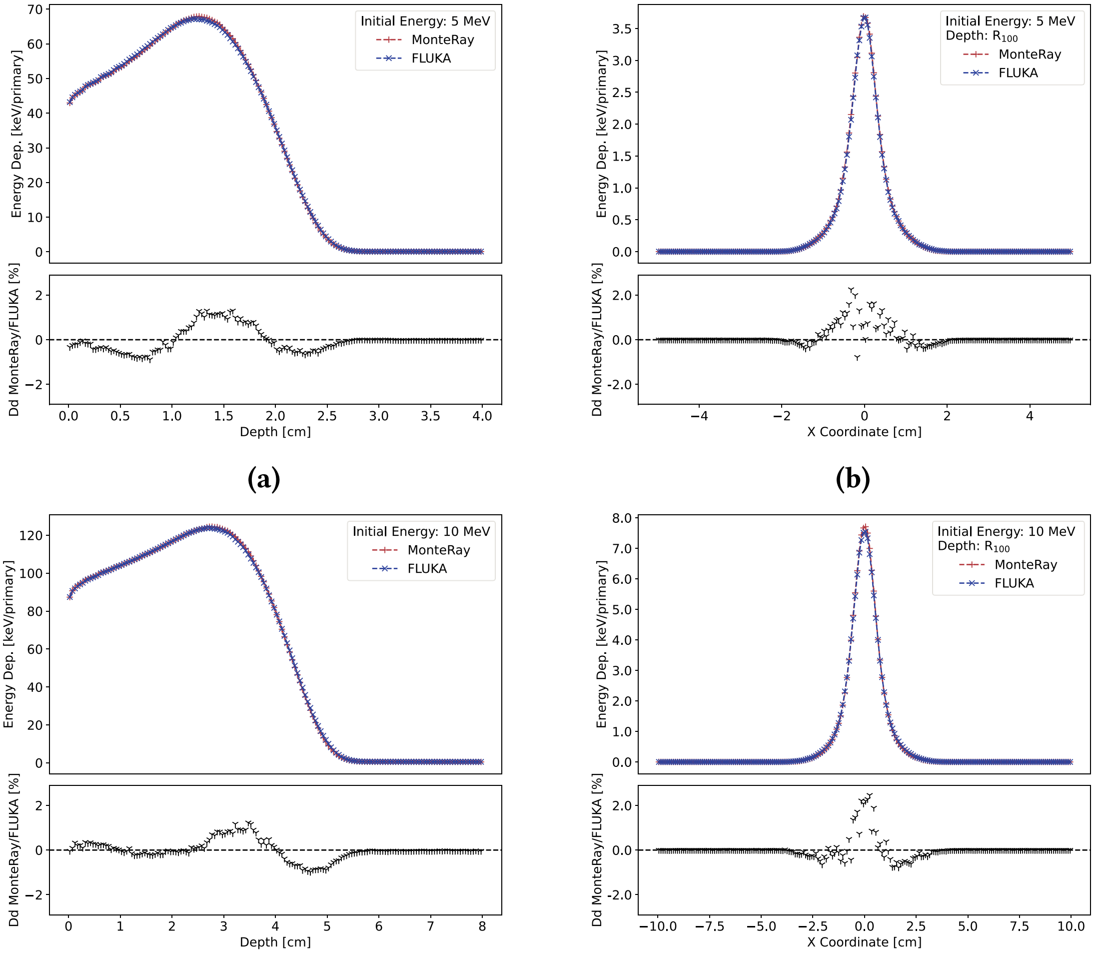

(a) **(b)**

(c) **(d)**

FIGURE 3 MR and FLUKA generated IDD curves (left panels) and lateral dose profiles (right panels) with corresponding dose differences in the lower panels for an electron pencil beam impinging on a water phantom with initial energies of 5 MeV (panel (a) and (b)) and 10 MeV (panel (c) and (d)). The simulations have been performed using 10^6 primary electrons. As the statistical uncertainties are below 1%, they are not reported in the figures. IDD, integrated depth dose.

Lateral profiles at the positions labeled with (A), (B), (C) and depth-dose profile at position (D) are also shown. MR and FLUKA are displayed with a solid and a dashed line, respectively. The results clearly demonstrate a high level of agreement between MR and FLUKA generated data. The local gamma passing rates (1%/1 mm, 5% cut-off) were 99.9% and 99.8% with the lung and bone insert, respectively. Using lower electron production and transport threshold of 10 keV in FLUKA compared to 100 keV as applied in all the FLUKA simulations here presented had no impact on the gamma passing rates.

In Figure 6, MR and FLUKA 2D dose distributions are overlaid on the CT of the anthropomorphic phantom. The 10 MeV electron beam (8 × 8 cm^2 field) impinges from the right side of the phantom. Depth-dose and lateral-dose profiles are shown at position (A) and (B), respectively. MR and FLUKA are displayed with a solid and a dashed line, respectively. The local gamma passing rate (3%/2 mm, 5% cut-off) was 99.4%.

3.2 | Experimental verification

3.2.1 | Modeling of the Mobetron electron linear accelerator head

The Mobetron incident electron beam parameters for FLUKA have been tuned such that simulated dose distributions in the water phantom positioned directly after the irradiation head match corresponding experimentally measured dosimetric data. A rectangular energy distribution with an energy spread of 1 MeV around a mean value of 9.4 MeV and a gaussian beam profile in the *x* and *y* direction with FWHM (full width at half maximum) = 0.1 cm was found to reproduce the measured

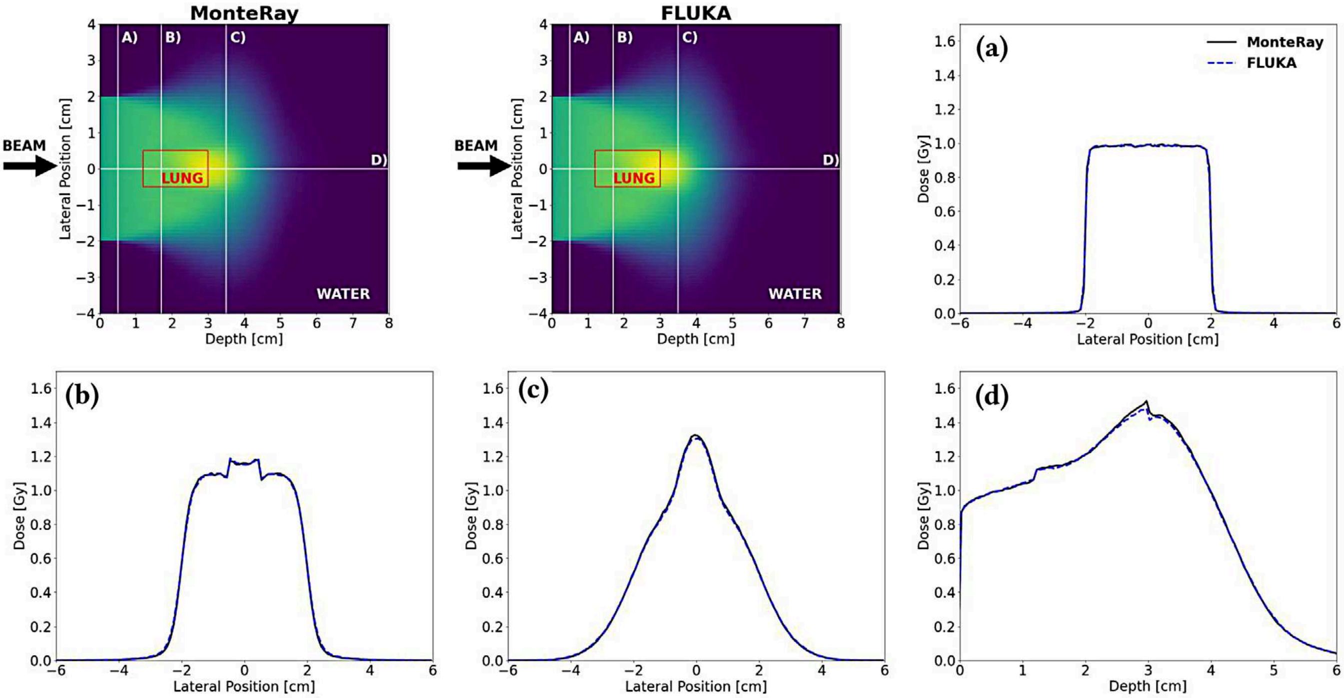

FIGURE 4 MR and FLUKA 2D dose distributions overlaid on the geometry: water tank with a lung insert. The 10 MeV electron beam (4×4 cm^2 field) impinges from the left side of the water tank as displayed with an arrow. Lateral profiles at the positions labeled with (A), (B), (C) and depth-dose profile at position (D) are also shown. MR and FLUKA are displayed with a solid and a dashed line, respectively. The simulations have been performed using 10^8 primary electrons. As the statistical uncertainties are below 1%, they are not reported in the figures. MR, MonteRay.

dose distributions best. A detailed summary of the electron and photon phase-space calculated with FLUKA is reported in the supplementary material (Figure S1).

3.2.2 | Benchmarking against dosimetric data

Dose distributions were generated with MR for particles sampled from the FLUKA-calculated Mobetron phase-space incident on a voxelized water geometry. The obtained results were then compared to FLUKA simulated dose distributions and measured data. To reach sufficiently low statistical uncertainties, 10^8 primary particles have been used to perform all MC simulations.

In Figure 7, the measured central axis depth dose distribution after the accelerator head as well as the corresponding FLUKA and MR generated results are shown. The MC derived dose curves were normalized such that the area under each simulated curve corresponds to the measured counterpart. In general, the MC generated results are in good agreement with the measured data. Dose differences within 3% for all investigated depths could be achieved. The average dose differences between MR (FLUKA) and the measurements were 1.3% (1.1%). Deviations between MR and FLUKA are well within 1.5% for all investigated depths and 0.6% on average. Therapeutic ranges (R_{80} depths), calculated based on the MR simulated, FLUKA generated and measured depth dose distributions are 30.67, 30.29, and 30.26 mm, respectively.

In Figure 8, the measured lateral dose profiles as well as the corresponding MC generated dose profiles are visualized for different depths in water: 3, 10, 15, 20, 25, and 37 mm. The presented results show a high level of agreement between the measured and simulated dose profiles. Dose differences between the simulated and measured data points are within 3 % for $>$ 99 % of all data points for both MR and FLUKA. The discrepancies between MR and FLUKA are within 1.5 % for 98.7 % of the data points.

Measuring errors and statistical uncertainties are not visualized in Figures 7 and 8 as they are below 1%. As for the simulations, the statistical uncertainties on the MR generated maximum dose values of the lateral profiles, shown in Figure 8, are within 0.5% for all investigated depths. The statistical uncertainties for FLUKA are in the same order of magnitude.

3.3 | Efficiency and timing performance

To benchmark MRs performance in the context of computing speed, end-to-end computing times were compared to FLUKA runtimes for pencil-like electron beams impinging on a sample geometry. In order to acquire precise computation times, all simulations have been performed 10 times with 10^6 primary particles. Timing performance has been obtained by simulating 5 and 10 MeV electron beams on a water phantom of $20 \times 20 \times 20$ cm^3 with 0.2 cm cubic scoring grid.[39] All simulations were executed on a single core using an Intel(R) Core(TM) i7-9700k processor. MR and FLUKA tracking rate, reported in primary/s, are respectively 124.9–10^3 and 7.7–10^3 for 5 MeV electrons and 67.0–10^3 and 5.1–10^3 for 10 MeV electrons. MR speed-up factors are about 16 and 13 for 5 and 10 MeV, respectively. Following Franciosini et al.[39] we have computed the MC simulation efficiency $\in = 1/(\sigma^2 T)$ where σ^2 is the simulation variance and T is the time calculation required to obtain this variance.[40] For each simulation setup, we computed the standard deviation σ of the maximum dose value of the longitudinal dose profile calculated on 10 independent MR and FLUKA runs of 10^6 electrons. The found statistical uncertainties were 0.086% (0.081%) for FLUKA 5(10) MeV and 0.085% (0.082%) for MR 5(10) MeV electron beams. Since the statistical uncertainties differ within about 1%, the efficiency comparisons are therefore equivalent to the calculation time ones.

4 | DISCUSSION

This work aims to present the development of an electron dose engine within MR, capable of estimating also dose distributions for Mobetron generated electron beams. The engine's performance was tested in terms of accuracy and simulation speed. Comparisons of MR predictions against corresponding FLUKA calculations and experimental data confirm that the developed engine can accurately simulate electron transport and interactions.

For the thin target calculations presented in Figure 2, differences between MR and FLUKA calculated mean energy loss values are 0.15% on average. Deviations of up to 2.4% from FLUKA simulations can be found in the literature for other electron MC engines, tested under similar conditions.[39] The MR derived mean scattering angles differ from corresponding FLUKA simulated values by up to $-2.7 \pm 0.6\%$ for 10 MeV electrons after 1 mm of water. Larger discrepancies of up to 5% from FLUKA simulations were reported previously for other electron MC frameworks.[39] However, from the angular distributions displayed in Figure 2b it is evident that the developed electron engine does not accurately reproduce the number of particles with intermediate scattering angles after 1 mm of water. This is a result of the scattering angle distribution being modeled via a piecewise-defined function consisting of a small angle approximation and a large angle approximation. No distinct sub function is implemented to describe intermediate scattering angles, resulting in noticeable inaccuracies in the angular distribution of electrons for thin layer thicknesses. These inaccuracies diminish when the traversed particle path is significantly longer than the MC step size. In that case, multiple single-step scattering angles add up to a total deflection angle for each particle, leading to a smoothed-out angular distribution, as can be seen from the MR generated angular distribution for 10 MeV electrons after 1 cm of water (see Figure 2d.)

The most important physical quantity in the context of radiation therapy is the deposited dose. The MR generated dose distributions for electron beams incident on a water phantom, displayed in Figure 3, match corresponding FLUKA calculated distributions within 2.3%, which is comparable to verification results presented previously for other electron MC engines.[39] A tolerance of 3% in the global dose difference is currently widely accepted as a clinical standard in the context of radiation therapy applications.[41] For 5 MeV electrons, differences between MR and FLUKA generated depth dose distributions are up to 1.5% while the simulation results for 10 MeV electrons exhibit a maximum dose difference of 1.0%.

Comparing MR and FLUKA predictions in presence of heterogeneity (Figures 4–6) confirmed the soundness of the models implemented in MR. A local gamma passing rate (3%/2 mm, low dose threshold of 5%) of 99.4% was obtained when using anthropomorphic phantom which is in line with the results of the other fast MC codes.[39]

Differences between MR calculated and measured dose values for Mobetron are below 3% for almost all investigated positions within the water phantom. For BEAMnrc[42] simulations of IORT electron beams, comparable dose differences were reported previously.[43] Optimizing the initial energy spectrum including a low energy electron tail as suggested in Alhamada et al.[44] could additionally improve the agreement with the experimental data.

Differences between the MR derived and FLUKA simulated dose distributions for Mobetron are within 1.5% for 98.8% of all data points, which reaffirms the accuracy of the developed electron dose engine. Nonetheless, the dose differences displayed in the lower panels of Figure 8 clearly illustrate that the MC generated Mobetron dose distributions systematically overestimate the dose at distances of approximately 40 mm from the central axis. Besides that, an underestimation of the dose occurs for distances of around 20 mm from the central axis. Those systematic errors could be due to the simplifications made in modeling the Mobetron generated radiation head and the initial beam distribution. However, it is important to notice that the impact of the slight systematic dose deviations on the width of the dose distributions is minimal. Deviations between the MC simulated and measured lateral dose profiles in terms of the

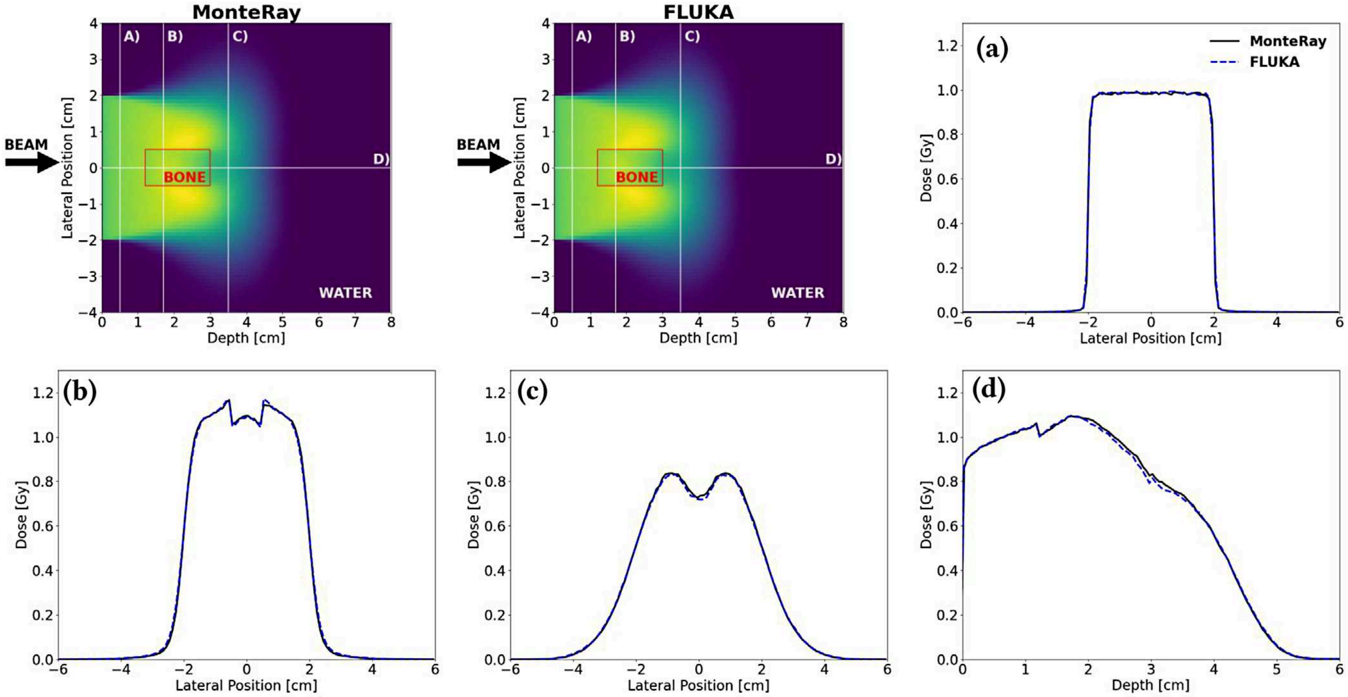

FIGURE 5 MR and FLUKA 2D dose distributions overlaid on the geometry: water tank with a bone insert. The 10 MeV electron beam (4×4 cm^2 field) impinges from the left side of the water tank as displayed with an arrow. Lateral profiles at the positions labeled with (A), (B), (C) and depth-dose profile at position (D) are also shown. MR and FLUKA are displayed with a solid and a dashed line, respectively. The simulations have been performed using 10^8 primary electrons. As the statistical uncertainties are below 1%, they are not reported in the figures. MR, MonteRay.

FWHM are below 1 mm for all investigated depths and below 0.1 mm at R_{50}.

As the beam model in FLUKA and consequently the phase space for MR was optimized to reproduce the experimental data, the comparisons shown in Figures 7 and 8 represent only an initial validation of MR. Additional comparisons with experimental data obtained in different conditions (different field size, source-to-skin (patient) distance, etc..) are needed for a comprehensive validation of MR for Mobetron.

Differences between the MC calculated and measured therapeutic ranges were determined, based on the Mobetron generated depth dose distributions presented in Figure 7. For both MC engines, the respective deviations are below 0.5 mm.

In contrast to depth dose distributions for pencil-like electron beams, the depth dose profiles for Mobetron generated beams in water exhibit no clear maximum. Instead, a plateau-like high-dose region can be identified for depths in water below ~ 25 mm. The same is true for the lateral dose distributions within that high-dose region. Here, relatively constant dose values can be observed for distances below ~20 mm from the central axis. These features of the Mobetron dose distributions are favorable for IORT and directly related to the characteristics of the Mobetron phase-space visualized in the Supplementary Material. The characteristics of the Mobetron phase-space, in turn, are a result of beam shaping and focusing mechanisms within the radiation head. In that context, it is worth noting that only ~17% of the particles in the phase-space are photons. For conventional non IORT electron accelerators, proportions of up to ~60% were reported in the literature.[45,46]

For dose calculations, general purpose MC frameworks such as FLUKA are considered the gold standard.[20] However, in the context of radiation therapy, and in particular of daily adaptive treatment, runtimes are a limiting factor concerning clinical applicability. This is why, besides accuracy, one of the main goals of the MR framework is fast simulation performance.[21–23] For the newly developed electron engine, the runtime analysis results for electron beam calculations presented in Section 3.3 show a reduction in computation times by a factor of approximately 16 and 13 with respect to FLUKA runtimes for 5 and 10 MeV electrons, respectively. Even though parallel execution of MR simulations on multiple cores is possible, just one core was used to benchmark the engine against FLUKA. Reductions in computation time by a factor of approximately 90 with respect to FLUKA simulations executed on a single core were reported recently for the GPU based MC electron framework FRED for 10 MeV electron.[39] For light ion calculations, MR computation times were found to scale linearly with the number of cores used.[21,22] Therefore, it

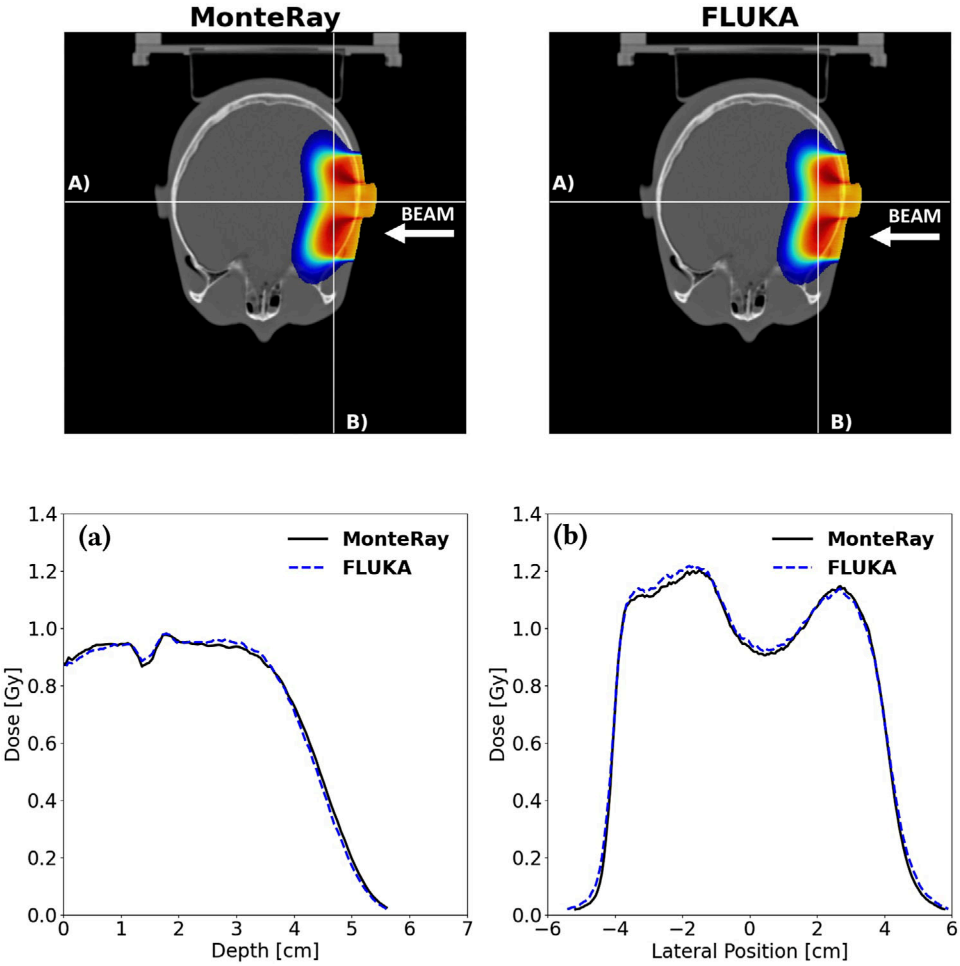

FIGURE 6 MR and FLUKA 2D dose distributions overlaid on the CT of the anthropomorphic phantom. The 10 MeV electron beam (8×8 cm^2 field) impinges from the right side of the phantom as displayed with an arrow. Depth-dose and lateral-dose profiles are shown at position (A) and (B), respectively. MR and FLUKA are displayed with a solid and a dashed line, respectively. The simulations have been performed using 4–10^8 primary electrons. As the statistical uncertainties are below 1%, they are not reported in the figures. MR, MonteRay.

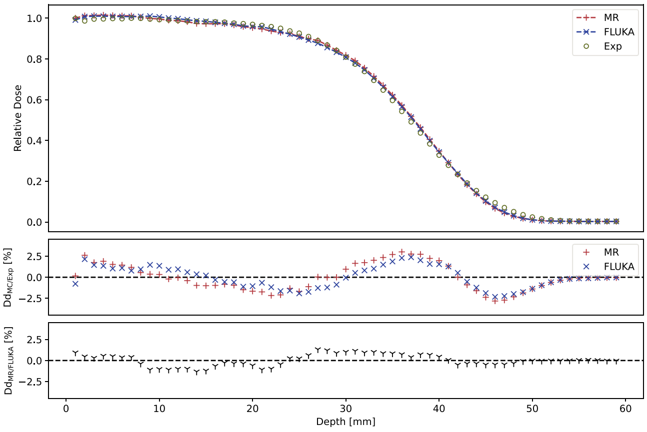

FIGURE 7 Experimentally measured percentage depth dose distribution after the Mobetron head versus FLUKA and MR generated results. The middle panel displays the dose differences between the MC simulated distributions and the measured data. The lower panel shows the dose differences between MR and FLUKA generated results. The simulations have been performed using 10^8 primary particles. Measuring errors and statistical uncertainties are below 1% and therefore not displayed. MC, MonteCarlo; MR, MonteRay.

is reasonable to assume that running MR electron simulations on 8 CPU cores would yield runtimes comparable to those of FRED. The found MR speed-up factor is mostly related to a simplified model for the multiples scattering, energy loss straggling and a tuned transport step-size approach.[28] However, two of the major bottlenecks concerning simulation speed are the scattering and energy loss routines. Approximately 20% of the total computation time for electron beam simulations using 10 MeV incident particles is spent on calculating continuous scattering angles. Sampling from the scattering angle distribution is computationally costly, even though approximations in favor of simulation speed have been made (see ref. 22). This is because complex functions have to be evaluated during runtime prior to calculating the scattering angle. Further approximations in the scattering routine might lead to faster runtimes; however, they would also cause reduced accuracy. Another ~20% of the total computation time is spent on calculating the continuous energy loss, since a multi-step sampling algorithm is employed to model energy loss

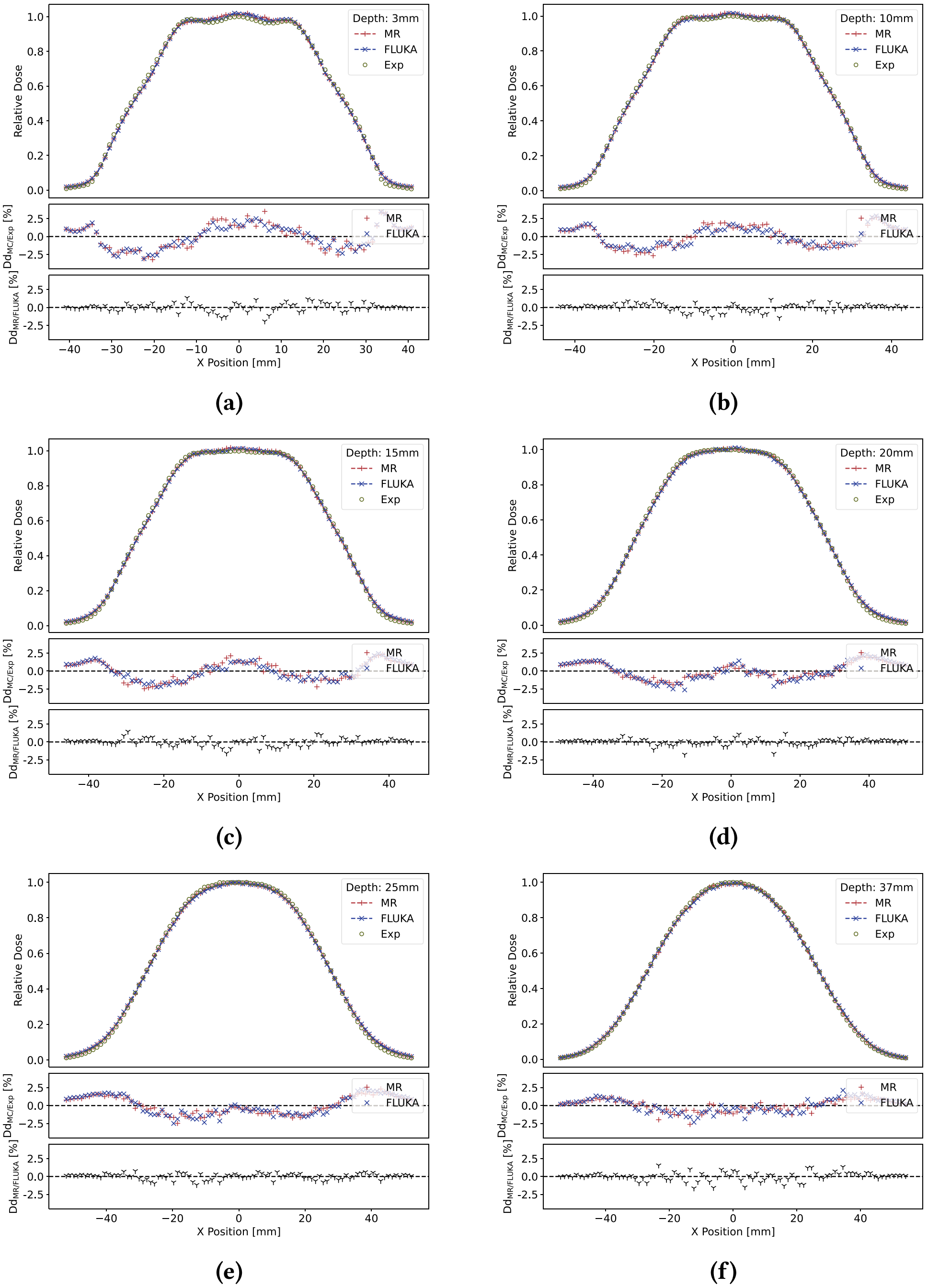

(a) (b) (c) (d) (e) (f)

FIGURE 8 Experimentally measured percentage lateral dose distributions after the Mobetron head versus FLUKA and MR generated results for different depths in water ranging from 3 mm (panel (a)) to 37 mm (panel (f)). The lower panels display the corresponding dose differences. The simulations have been performed using 10^8 primary particles. Measuring errors and statistical uncertainties are below 1% and therefore not displayed. MR, MonteRay.

fluctuations. The electron specific submodules do not add significantly to the simulation time: the CPU time spent in the bremsstrahlung, Møller and Compton routines corresponds to ~2% of the total computation time.

A future perspective for the developed electron engine might be GPU acceleration, which has the potential to substantially enhance runtimes. Also, an interface with biophysical models[9–11] to accurately predict pre-clinical in vitro and in vivo experiments is possible. Integration of dose-rate predictions are underway to enable FLASH IORT calculations based on the Mobetron accelerator.

5 | CONCLUSIONS

In the scope of this work, the existing fast MC framework MR, designed for proton, helium ion, and carbon ion dose calculations, was extended to allow for electron beam simulations. Besides electron and photon interactions with matter, a beam model specific to the Mobetron electron linear accelerator was incorporated within MR to enable dose calculations for Mobetron generated electron beams. To assess its accuracy and performance, the developed electron dose engine was extensively benchmarked against FLUKA calculations and dosimetric data. Excellent agreement was found for comparisons of MR generated dose distributions against FLUKA calculations in water and in the presence of heterogeneities. Similarly, good results, that is, dose differences within ∼3%, were observed when evaluating the MR simulations against the measured dose distributions. In terms of simulation speed, 13 times the speed of FLUKA was attained for 10 MeV electrons.

ACKNOWLEDGMENTS

The authors would like to acknowledge the support provided by IntraOP. The authors acknowledge financial support through the German Federal Ministry of Education and Research (BMBF) (Grant number: 13GW0436A). The authors would like to thank Alberto Fassò for providing tabulated values of Seltzer and Berger in electronic form.

Open access funding enabled and organized by Projekt DEAL.

CONFLICT OF INTEREST STATEMENT

The authors declare no conflicts of interest.

REFERENCES

1. Sung H, Ferlay J, Siegel RL, et al. Global cancer statistics 2020: gLOBOCAN estimates of incidence and mortality worldwide for 36 cancers in 185 countries. *CA Cancer J Clin*. 2021;71(3):209-249. doi:10.3322/caac.21660
2. Durante M, Loeffler JS. Charged particles in radiation oncology. *Nat Rev Clin Oncol*. 2010;7(1):37-43. doi:10.1038/nrclinonc.2009.183
3. Baskar R, Lee KA, Yeo R, Yeoh KW. Cancer and radiation therapy: current advances and future directions. *Int J Med Sci*. 2012;9(3):193-199. doi:10.7150/ijms.3635
4. Salguero FJ, Arráns R, Palma BA, Leal A. Intensity- and energy-modulated electron radiotherapy by means of an xMLC for head and neck shallow tumors. *Phys Med Biol*. 2010;55(5):1413-1427. doi:10.1088/0031-9155/55/5/010
5. Meurk ML, Goer DA, Spalek G, Cook T. The Mobetron: a new concept for IORT. *Front Radiat Ther Oncol*. 1997;31:65-70.
6. Favaudon V, Caplier L, Monceau V, et al. Ultrahigh dose-rate FLASH irradiation increases the differential response between normal and tumor tissue in mice. *Sci Transl Med*. 2014;6(245):245ra93. doi:10.1126/scitranslmed.3008973
7. Montay-Gruel P, Petersson K, Jaccard M, et al. Irradiation in a flash: unique sparing of memory in mice after whole brain irradiation with dose rates above 100 Gy/s. *Radiother Oncol*. 2017;124(3):365-369. doi:10.1016/j.radonc.2017.05.003
8. Vozenin M-C, De Fornel P, Petersson K, et al. The advantage of FLASH radiotherapy confirmed in mini-pig and cat-cancer patients. *Clin Cancer Res*. 2019;25(1):35-42. doi:10.1158/1078-0432.CCR-17-3375
9. Liew H, Mein S, Dokic I, et al. Deciphering time-dependent DNA damage complexity, repair, and oxygen tension: a mechanistic model for FLASH-dose-rate radiation therapy. *Int J Radiat Oncol*. 2021;110(2):574-586. doi:10.1016/j.ijrobp.2020.12.048
10. Liew H, Mein S, Tessonnier T, et al. The impact of sub-millisecond damage fixation kinetics on the in vitro sparing effect at ultra-high dose rate in UNIVERSE. *Int J Mol Sci*. 2022;23(6):2954. doi:10.3390/ijms23062954
11. Liew H, Mein S, Tessonnier T, et al. Do we preserve tumor control probability (TCP) in FLASH radiotherapy? a model-based analysis. *Int J Mol Sci*. 2023;24(6):5118. doi:10.3390/ijms24065118
12. Ferrari A, Paola S, Fasso A, Ranft J. FLUKA: A *Multi-Particle Transport Code (Program Version 2005)*. CERN; 2005. doi:10.5170/CERN-2005-010
13. Ferrari A, et al. FLUKA: A multi-particle transport code (program version 2023)." Accessed: Aug. 19, 2023. [Online]. Available: http://www.fluka.org/content/manuals/FM.pdf
14. Battistoni G, Boehlen T, Cerutti F, et al. Overview of the FLUKA code. *Ann Nucl Energy*. 2015;82:10-18. doi:10.1016/j.anucene.2014.11.007
15. Agostinelli S, Allison J, Amako K, et al. Geant4—a simulation toolkit. *Nucl Instrum Methods Phys Res Sect Accel Spectrometers Detect Assoc Equip*. 2003;506(3):250-303. doi:10.1016/S0168-9002(03)01368-8
16. Geant4 Collaboration. Physics reference manual. Accessed: Sep. 24, 2023. [Online]. Available: https://indico.cern.ch/event/679723/contributions/2792554/attachments/1559217/2454299/PhysicsReferenceManual.pdf
17. Baró J, Sempau J, Fernández-Varea JM, Salvat F. PENELOPE: an algorithm for Monte Carlo simulation of the penetration and energy loss of electrons and positrons in matter. *Nucl Instrum Methods Phys Res Sect B Beam Interact Mater At*. 1995;100(1):31-46. doi:10.1016/0168-583X(95)00349-5
18. PENELOPE-2018: a code system for Monte Carlo simulation of electron and photon transport, workshop proceedings. Accessed: Sep. 24, 2023. [Online]. Available: https://www.oecd-nea.org/upload/docs/application/pdf/2020-10/penelope-2018__a_code_system_for_monte_carlo_simulation_of_electron_and_photon_transport.pdf
19. Kawrakow I. Accurate condensed history Monte Carlo simulation of electron transport. I. EGSnrc, the new EGS4 version. *Med Phys*. 2000;27(3):485-498. doi:10.1118/1.598917
20. Fielding AL. Monte-Carlo techniques for radiotherapy applications I: introduction and overview of the different Monte-Carlo codes. *J Radiother Pract*. 2023;22:e80. doi:10.1017/S1460396923000079
21. Lysakovski P, Ferrari A, Tessonnier T, et al. Development and benchmarking of a Monte Carlo dose engine for proton radiation therapy. *Front Phys*. 2021;9:741453. doi:10.3389/fphy.2021.741453
22. Lysakovski P, Besuglow J, Kopp B, et al. Development and benchmarking of the first fast Monte Carlo engine for helium ion beam dose calculation: MonteRay. *Med Phys*. 2022;50(4):2510-2524. doi:10.1002/mp.16178
23. Lysakovski P, Kopp B, Tessonnier T, et al. Development and validation of MonteRay, a fast Monte Carlo dose engine for carbon ion beam radiotherapy. *Med Phys*. 2023;51(2):1433-1449. doi:10.1002/mp.16754
24. Chibani O. New algorithms for the Vavilov distribution calculation and the corresponding energy loss sampling. *IEEE Trans Nucl Sci*. 1998;45(5):2288-2292. doi:10.1109/23.725266
25. Pauli W. Über den Zusammenhang des Abschlusses der Elektronengruppen im Atom mit der Komplexstruktur der Spektren. *Zeitschrift Für Phys*. 1925;31(1):765-783. doi:10.1007/BF02980631
26. Molière G. Theorie der Streuung schneller geladener Teilchen II Mehrfach-und Vielfachstreuung. *Zeitschrift Für Naturforschung A*. 1948;3(2):78-97. doi:10.1515/zna-1948-0203
27. Kuhn SE, Dodge GE. A fast algorithm for Monte Carlo simulations of multiple coulomb scattering. *Nucl Instrum Methods Phys Res*

Sect Accel Spectrometers Detect Assoc Equip. 1992;322(1):88-92. doi:10.1016/0168-9002(92)90361-7

28. Sempau J, Wilderman SJ, Bielajew AF. DPM, a fast, accurate Monte Carlo code optimized for photon and electron radiotherapy treatment planning dose calculations. *Phys Med Biol*. 2000;45(8):2263-2291. doi:10.1088/0031-9155/45/8/315
29. Salvat F, Fernández-Varea J. Semiempirical cross sections for the simulation of the energy loss of electrons and positrons in matter. *Nucl Instrum Methods Phys Res Sect B Beam Interact Mater At*. 1992;63(3):255-269. doi:10.1016/0168-583X(92)95108-4
30. Seltzer SM, Berger MJ. Bremsstrahlung spectra from electron interactions with screened atomic nuclei and orbital electrons. *Nucl Instrum Methods Phys Res Sect B Beam Interact Mater At*. 1985;12(1):95-134. doi:10.1016/0168-583X(85)90707-4
31. Wasaye MA, Wang H, He P. An algorithm for Monte Carlo simulation of bremsstrahlung emission by electrons. *Nucl Sci Tech*. 2017;28(5):71. doi:10.1007/s41365-017-0218-7
32. Berger MJ, Hubbell JH. *XCOM: photon cross sections on a personal computer*. National Bureau of Standards, Washington, DC (USA). Center for Radiation Research, NBSIR-87-3597; 1987. doi:10.2172/6016002
33. Klein O, Nishina Y. Über die Streuung von Strahlung durch freie Elektronen nach der neuen relativistischen Quantendynamik von Dirac. *Zeitschrift Für Phys*. 1929;52(11):853-868. doi:10.1007/BF01366453
34. Bethe H, Heitler W, Dirac PAM. On the stopping of fast particles and on the creation of positive electrons. *Proc R Soc A*. 1934;146(856):83-112. doi:10.1098/rspa.1934.0140
35. Tsai Y-Su. Pair production and bremsstrahlung of charged leptons. *Rev Mod Phys*. 1974;46(4):815-851. doi:10.1103/RevModPhys.46.815
36. Heitler W. *Quantum Theory Of Radiation*. Oxford University Press; 1954.
37. Motz JW, Olsen HA, Koch HW. Pair production by photons. *Rev Mod Phys*. 1969;41(4):581-639. doi:10.1103/RevModPhys.41.581
38. IntraOp. FLASH radiotherapy—ultra-high dose rates (UHDR) w/Electrons. IntraOp. Accessed: Aug. 09, 2023. [Online]. Available: https://intraop.com/flash-radiotherapy-electrons/
39. Franciosini G, Battistoni G, Cerqua A, et al. GPU-accelerated Monte Carlo simulation of electron and photon interactions for radiotherapy applications. *Phys Med Biol*. 2023;68(4):044001. doi:10.1088/1361-6560/aca1f2
40. Chetty IJ, Curran B, Cygler JE, et al. Report of the aapm task group no. 105: issues associated with clinical implementation of monte carlo-based photon and electron external beam treatment planning. *Med Phys*. 2007;34:4818-4853. doi:10.1118/1.2795842
41. Baran M, Kabat D, Tulik M, Rzecki K, Sośnicki T, Tabor Z. Statistical approach to the selection of the tolerances for distance to agreement improves the quality control of the dose delivery in radiotherapy. *Phys Med Biol*. 2020;65(14):145004. doi:10.1088/1361-6560/ab86d5
42. Rogers DWO, Walters B, Kawrakow I. BEAMnrc users manual. *NRC Rep PIRS*. 2001;509:12
43. Lazarus GL, Van Eeden D, Du Plessis FCp. Validation of Monte Carlo-based calculations for megavolt electron beams for IORT and FLASH-IORT. *Heliyon*. 2022;8(9):e10682. doi:10.1016/j.heliyon.2022.e10682
44. Alhamada H, Simon S, Philippson C, et al. Monte Carlo dose calculations of shielding disks with different material combinations in intraoperative electron radiation therapy (IOERT). *Cancer/Radiothérapie*. 2020;24(2):128-134. doi:10.1016/j.canrad.2020.02.006
45. Righi S, Karaj E, Felici G, Di Martino F. Dosimetric characteristics of electron beams produced by two mobile accelerators, Novac7 and Liac, for intraoperative radiation therapy through Monte Carlo simulation. *J Appl Clin Med Phys*. 2013;14(1):6-18. doi:10.1120/jacmp.v14i1.3678
46. Ding GX, Rogers DWO. Energy spectra, angular spread and dose distributions of electron beams from various accelerators used in radiotherapy. *Natl Res Counc Can Inst Natl Meas Stand*. 1995.

SUPPORTING INFORMATION

Additional supporting information can be found online in the Supporting Information section at the end of this article.

How to cite this article: Rank L, Lysakovski P, Major G, et al. Development and verification of an electron Monte Carlo engine for applications in intraoperative radiation therapy. *Med Phys*. 2024;51:6348–6364. https://doi.org/10.1002/mp.17180